USGS
science for a changing world

Prepared for the National Aeronautics and Space Administration

Bedrock and Structural Geologic Maps of Eastern Candor Sulci, Western Ceti Mensa, and Southeastern Ceti Mensa, Candor Chasma, Valles Marineris Region of Mars

By Chris H. Okubo and Tenielle A. Gaither

Pamphlet to accompany
Scientific Investigations Map 3359

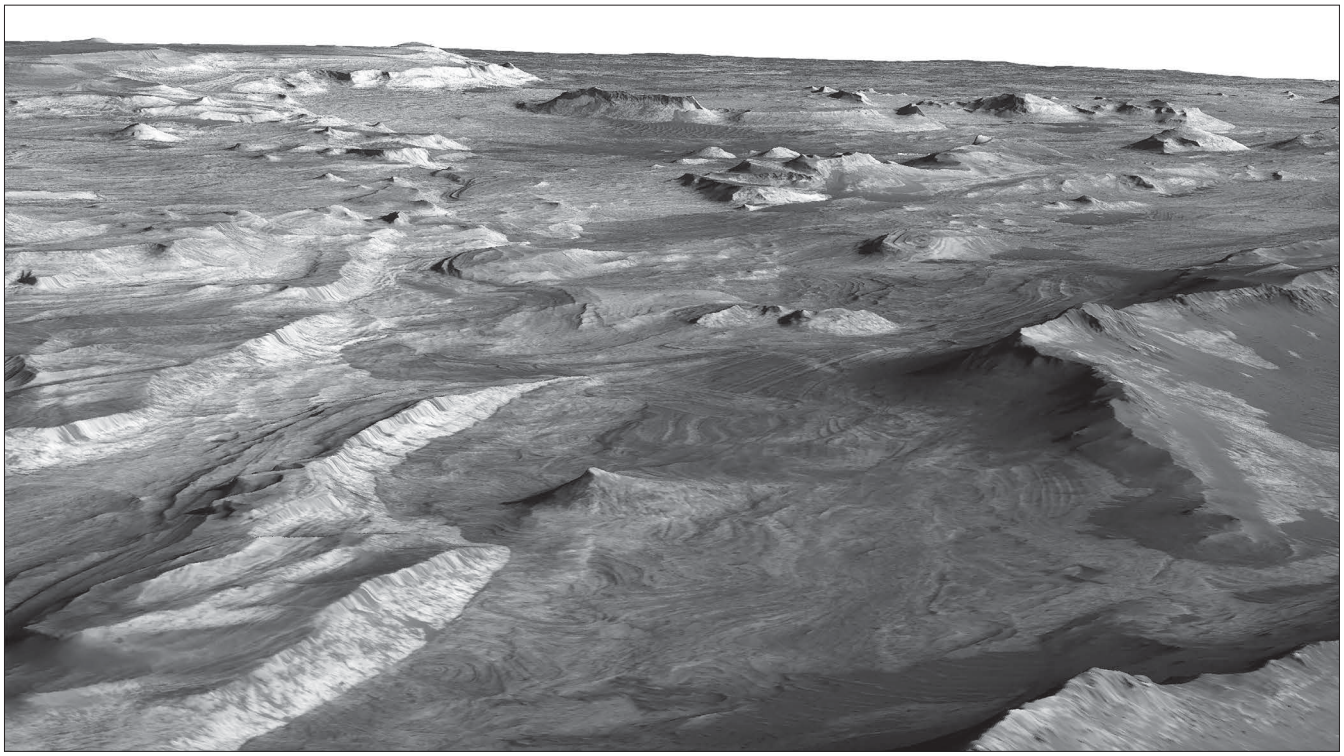

View of west Ceti Mensa map area looking toward the southeast from a vantage point near lat 5.65° S., long 283.50° E., showing widespread outcrops of stratified bedrock. High Resolution Science Experiment (HiRISE) observation PSP_002841_1740 overlain on the HiRISE digital elevation model (DEM).

2017

U.S. Department of the Interior
U.S. Geological Survey

Contents

Figures

Tables

Introduction

This map product contains a set of three 1:18,000-scale maps showing the geology and structure of study areas in the western Candor Chasma region of Valles Marineris, Mars. These maps are part of an informal series of large-scale maps and map-based topical studies aimed at refining current understanding of the geologic history of western Candor Chasma. The map bases consist of digital elevation models and orthorectified images derived from High Resolution Imaging Science Experiment (HiRISE) data. These maps are accompanied by geologic cross sections, colorized elevation maps, and cutouts of HiRISE images showing key superposition relations. Also included in this product is a Correlation of Map Units that integrates units across all three map areas, as well as an integrated Description of Map Units and an integrated Explanation of Map Symbols. The maps were assembled using ArcGIS software produced by Environmental Systems Research Institute (http://www.esri.com). The ArcGIS projects and databases associated with each map are included online as supplemental data.

Background

Valles Marineris is located in the western equatorial region of Mars. This 4,000-km-long network of interconnected canyons was discovered in images acquired by the Mariner 9 television experiment in 1972 (McCauley and others, 1972). The Mariner 9 images were acquired at resolutions of 1–3 km globally and at resolutions of 100–300 meters (m) across less than 2 percent of the planet. Using these data, the first global shaded-relief map of Mars was constructed at a scale of 1:25,000,000 (Bridges and Inge, 1972) and controlled photomosaics at scales up to 1:5,000,000 were created (Batson and others, 1979).

The Mariner 9 data revealed that many canyons in Valles Marineris contain prominently stratified rocks that have an albedo higher than that of the bedrock exposed in the chasma walls (but moderate overall for Mars). Masursky (1973) interpreted these stratified rocks as valley-fill deposits. Subsequently, McCauley (1978) used the Mariner 9 data to construct a geologic map of Valles Marineris at a scale of 1:5,000,000. McCauley (1978) interpreted the chasmata's wall rock as bedrock of unspecified origin and divided the surrounding plains into four geologic units consisting of materials such as flood lavas, loess, or ash. The stratified, moderate-albedo rocks were classified as "layered chasma material" and were interpreted to consist of lacustrine sediments that were deposited within the chasma, eroded by large floods, and then recently modified by eolian activity. McCauley (1978) also recognized a "chasma floor material" unit within Valles Marineris and suggested that this unit was composed of mass-wasting deposits derived from the chasma walls and covered by fluvial sediments.

Scott and Carr (1978) compiled the results of McCauley (1978) and other Mariner-based geologic map quadrangles and produced a global geologic map. The map of Scott and Carr (1978) is notable because it proposed a new Martian chronostratigraphic system—the same system that is used today. Scott and Carr (1978) divided the rock exposed along chasma walls and on the surrounding volcanic plains into three units consisting of lava flows with a minor component of impact breccia. They assigned ages of Late Noachian to Early Amazonian to these units. All floor materials of Valles Marineris were collectively classified as Late Hesperian to Early Amazonian and interpreted as fluvial, eolian, and mass-wasting deposits.

Geologic maps of Valles Marineris were subsequently updated with data from visual imaging subsystem (VIS) cameras on board the Viking 1 and 2 orbiters. Scott and Tanaka (1986) produced a 1:15,000,000-scale geologic map of the western equatorial region of Mars (including Valles Marineris) by using VIS data acquired at 130–300 m/pixel. The "Layered Chasma Material" and "Chasma Floor Material" unit groupings of McCauley (1978) were renamed the "Layered Material" and "Floor Material" groupings, respectively, and the geologic interpretations of McCauley (1978) were maintained for these units. Scott and Tanaka (1986) interpreted the chasma wall rock to be Noachian to Middle Hesperian and the surrounding plains materials to be Noachian to Late Hesperian. Scott and Tanaka (1986) also interpreted the "Layered Material" unit to be Late Hesperian and the "Floor Material" unit to be Early Amazonian.

Witbeck and others (1991) used VIS data at resolutions of 30–150 m/pixel to revise earlier geologic mapping in the Valles Marineris area with a primary focus on mapping chasmata floor materials. In this 1:2,000,000-scale map, Witbeck and others (1991) largely adopted unit ages, distributions, and interpretations of chasma wall rock and surrounding plains from Scott and Tanaka (1986). Witbeck and others (1991) divided the stratified, moderate-albedo rocks within the chasmata into one Late Hesperian "Layered material" unit and three Late Hesperian to Amazonian "Massive deposits" units. The "Layered material" unit was interpreted to be volcanic or lacustrine sediment deposited within the chasmata. Units within the "Massive deposits" grouping were interpreted as volcanic or eolian sediments, possibly accompanied by sediment derived from the "Layered material" unit. Four "Floor materials" units were also recognized and were interpreted to consist of Late Hesperian to Amazonian alluvial, eolian, and mass-wasting deposits.

Parts of central Valles Marineris were subsequently mapped at 1:500,000 scale using VIS data. These maps were notable for presenting a significant increase in the level of detail of mapped units and structures compared to previous smaller-scale geologic maps of the area (Schultz, 1998a; Lucchitta, 1999). These larger-scale maps presented a diverse set of geologic units, with ages and interpretations generally supporting the results of previous works. Mapped structures included wrinkle ridges and graben in the plains surrounding the chasma; normal faults within the chasma wall rock; and layers, normal faults, scarps, and ridges within the stratified moderate-albedo rocks on the chasma floor. Results of this large-scale mapping supported hypotheses that normal faulting and rifting played a key role in the structural evolution of Valles Marineris (for example, Peulvast and Masson, 1993; Schultz, 1998b; Schultz and Lin, 2001).

Recently, Tanaka and others (2014) produced an updated global geologic map of Mars at 1:20,000,000 scale by using data acquired since the Viking missions and by incorporating

results from previous mapping and thematic studies. This mapping primarily used data from a global digital elevation model (DEM) that is based on data from the Mars Orbiter Laser Altimeter (MOLA; 463 m/pixel at the equator) on board the Mars Global Surveyor (Smith and others, 2001). Global mosaics of daytime and nighttime infrared data from the Thermal Emission Imaging System (100 m/pixel) on board the Mars Odyssey (Christensen and others, 2004) and images from the Context Camera (CTX; 5 to 6 m/pixel) on board the Mars Reconnaissance Orbiter (MRO; Malin and others, 2007) were also used. Tanaka and others (2014) interpreted the chasma wall rock to consist of Noachian sedimentary, impact, and volcanic materials. The surrounding plains were divided into a variety of units ranging from Early Noachian to Late Hesperian and comprising flood lavas and lava flows, as well as volcaniclastic, impact, fluvial, eolian, and other sedimentary materials. The stratified, moderate-albedo rocks within Valles Marineris were interpreted as Hesperian eolian deposits or pyroclastic air-fall deposits. Other materials on the floor and lower walls of the chasmata were interpreted as Late Hesperian fluviolacustrine and mass-wasting deposits, as well as Middle to Late Amazonian mass-wasting deposits.

Combined, these recent map-based investigations and contemporary thematic studies, including structural analyses using data from the High-Resolution Stereo Camera (HRSC; 2 and 10 m/pixel) on board the Mars Express (Fueten and others, 2006, 2008, 2014; Jaumann and others, 2007; Birnie and others, 2012), provide the following generalized geology history for this region:

(1) Middle to Late Noachian Epochs—Rift systems developed in Noachian volcanic, impact, and sedimentary sequences that are presently exposed along the chasma walls and make up the bulk of the Thaumasia highlands. These rifts were the nascent stages of Valles Marineris formation and may have developed in response to growth of the Tharsis rise. Rifting was accompanied by increased local volcanic activity.

(2) Late Noachian to Early Hesperian Epochs—Rifting and volcanism became prominent and aerially extensive. Graben and pit chains began to form and were subsequently modified by fluvial erosion and mass wasting. Flood lavas, lava flows, and pyroclastic deposits blanketed the surrounding plains, and volcanism migrated westward. Large floods of water were discharged from basins, fissures, and pits in Valles Marineris, and large-scale outflow channels formed to the east. The stratified, moderate-albedo rocks began to accumulate as sedimentary deposits within Valles Marineris as well as on the surrounding plains.

(3) Hesperian Period—Major rifting and volcanism continued to migrate westward, forming the Syria Planum and Noctis Labyrinthus regions. Rift-related normal faults deformed sedimentary rocks within Valles Marineris. Sedimentary deposits continued to accumulate within Valles Marineris at diminished rates after cessation of rifting. Chasmata floors were covered by landslides, debris flows, and other mass-wasting deposits derived not only from the chasma walls but also from the sedimentary deposits.

(4) Amazonian Period—Volcanism continued to migrate westward, forming the Tharsis rise. Accumulation of sedimentary deposits ceased within Valles Marineris, while mass-wasting deposits continued to accumulate on the floors and lower walls of the chasmata. Eolian erosion became the dominant geologic process continuing into the present.

Though most map-based investigations and thematic studies supported this generalized geologic history of Valles Marineris, two fundamental issues remained contentious: (1) various lines of evidence supported an alternative interpretation that deposition of some sedimentary rocks exposed within Valles Marineris predated chasma formation (for example, Malin and Edgett, 2000, 2001; Montgomery and Gillespie, 2005; Catling and others, 2006); (2) the provenance of these sedimentary rocks was also debated. Interpretations included origins as aeolian, pyroclastic, hyaloclastic, fluvial-deltaic, playa deposits or combinations thereof (for example, McCauley, 1978; Peterson, 1981; Nedell and others, 1987; Lucchitta and others, 1992; Chapman and Tanaka, 2001; Dromart and others, 2007; Murchie and others, 2009a; Fueten and others, 2014); diagenetic alteration of these sediments (Mangold and others, 2008; Murchie and others, 2009a) likely mask their original mineral composition.

Recently, unprecedented high-resolution images, acquired by the High Resolution Imaging Science Experiment (HiRISE; 0.25 m/pixel) on board the Mars Reconnaissance Orbiter (MRO) (McEwen and others, 2010) enabled more detailed testing of prevailing models for the geologic history of Valles Marineris, as well as topical investigations into the timing of sediment deposition relative to chasma formation and depositional environments. Principally, the high resolution and stereo capability of HiRISE allowed new meter-scale observations, such as (1) superposition relations between sediments and chasma wall rock to test the relative ages of sedimentation and chasma formation, (2) crosscutting relations between rift-related normal faults and sediments to test the relative ages of sedimentation and rifting, and (3) depositional structures within sediments to constrain the depositional environment.

Okubo and others (2008) and Okubo (2010) were the first to employ HiRISE stereo images and DEMs to conduct high-resolution structural mapping of Hesperian sedimentary rocks (Tanaka and others, 2014) within the Chasma region of Valles Marineris (fig. 1). They used HiRISE DEMs with 1-m post spacings and orthorectified images at 0.25 m/pixel. Their structural mapping, at a scale of 1:24,000, revealed that local sediments were not deformed by faults related to chasma formation, even though such faults were predicted there (Schultz and Lin, 2001). This finding was consistent with the hypothesis that rifting within this part of Valles Marineris had ceased during the Hesperian and that sedimentation continued after rifting. Further, Okubo and others (2008) and Okubo (2010) showed that orientations of stratigraphic layers supported interpretations that sediments accumulated as basin fill and were deposited after the Chasma had formed. These maps also revealed that sediments experienced kilometer-scale landsliding.

Recently, Okubo (2014) produced a 1:18,000-scale structural and geologic map of Hesperian sedimentary rocks (Tanaka and others, 2014) in the Candor Colles region of the Chasma (fig. 1). This mapping again used a HiRISE DEM with 1-m post spacings and orthorectified images at 0.25 m/pixel. This work

showed that sedimentary rocks in this region were deposited in a wet playa-like environment within western Candor Chasma, and that deposition was periodically interrupted by formation of regional erosional surfaces attributed to eolian deflation. These erosional surfaces are preserved as prominent unconformities that bound allostratigraphic units. Further, the accumulating sediments were subjected to kilometer-scale syndepositional landsliding. Okubo (2014) argued that these landslides triggered soft-sediment deformation, including the formation of injectite megapipes, which are 10- to 100-m-scale bodies of sediments that were mobilized within the subsurface (for example, Chan and others, 2007). All observed deformation was attributed to these slope failures and soft-sediment deformation, and no evidence of chasma-related faulting was found.

The works of Okubo and others (2008) and Okubo (2010, 2014) constituted an informal series of large-scale maps and map-based topical studies aimed at refining current understanding of the geologic history of western Candor Chasma. Though insightful, these works examined a few, relatively small areas (fig. 1) and, consequently, large-scale maps in other strategic areas of western Candor Chasma were needed to build a representative geologic history for the region. The stratigraphy above and below the stratigraphic sequence studied by these earlier works needed characterization to understand the variety of depositional environments that were present in different areas of the chasma and whether these environments changed over time. Further, the occurrence and relative ages of deformational features, such as soft-sediment deformation and landslides (for example, Okubo, 2014), or faults related to chasma formation (Schultz and Lin, 2001), needed to be established at more broadly distributed areas to assess their significance in the broader history of the chasma.

Strategic areas for additional large-scale mapping in western Candor Chasma were identified on the basis of structure and stratigraphy identified in CTX images. Unit contacts (regional unconformities) identified by Okubo (2014) were traced laterally throughout western Candor Chasma and revealed key stratigraphic exposures above and below the previously studied stratigraphic sequence. Areas where predicted traces of chasma-related normal faults (Schultz and Lin, 2001) intersected the oldest sedimentary units identified by Witbeck and others (1991) were considered high priority. Candidate map locations were also constrained by the availability of HiRISE stereo images of suitable quality to create DEMs. Finally, CTX images were used to find areas of low strain, where deformational features represent local structure but are not so highly deformed that the local stratigraphy cannot be reconstructed.

Our analysis revealed three high-priority areas for additional large-scale (1:18,000) mapping within western Candor Chasma (fig. 1). The eastern Candor Sulci map area is in a region where sedimentary rocks are exposed in a series of subparallel ridges and troughs. This map area covers the contact between the layered sedimentary deposits on the floor of western Candor Chasma and the wall rock of the chasma's northern escarpment. Two additional map areas, the southeastern and western Ceti Mensa, are on Ceti Mensa, a broad, high-standing mesa of stratified sedimentary rock. The southeastern Ceti Mensa map area contains an eastward extension of the Candor Colles unit of Okubo (2014), as well as strata that underlies, and strata that buries, the entire stratigraphic sequence of Okubo (2014). The western Ceti Mensa map area contains geologic units that were deposited near the summit of Ceti Mensa. These units overlie the stratigraphic sequence of Okubo (2014) and are among the youngest sedimentary deposits in the chasma.

The results of mapping in these three areas are presented in this report. Additionally, these new results are integrated with the previous work of Okubo and others (2008), Okubo (2010, 2014), and a geologic history for the broader western Candor Chasma region is proposed herein.

Map Base and Data

All three maps are in Transverse Mercator projection with a central meridian of 285° E. The primary datasets used in mapping were stereo HiRISE observations (table 1). For each map area, a DEM with 1-m post spacing was constructed from the red bandpasses (550–850 nm) of the respective HiRISE stereo observations. Each HiRISE image was then orthorectified to the DEM, output at 1 m/pixel and 0.25 m/pixel, and compressed using the JPEG2000 image compression standard. The DEM production and image orthorectification process followed the methodology outlined by Kirk and others (2008). All data used in the construction of these maps were obtained from the National Aeronautics and Space Administration (NASA) Planetary Data System.

The precision of elevation values in the HiRISE DEMs used in these maps was estimated on the basis of viewing geometry and pixel scale. The image pair used for the southeastern Ceti Mensa map area, ESP_012295_1730 (0.282 m/pixel) and ESP_011372_1730 (0.263 m/pixel), had a 15.3° stereoscopic convergence angle. Assuming 1/5 pixel matching error and 0.282 m/pixel in the more oblique image, the vertical precision for this DEM was estimated as $0.282/5/\tan(15.3°) = 0.21$ m (for example, Kirk and others, 2008). Similarly, the DEMs for the western Ceti Mensa and eastern Candor Sulci map areas had estimated vertical precisions of 0.12 m and 0.21 m, respectively. Comparison of overlapping HiRISE DEMs created in the same way, in support of landing site selection for the Mars Science Laboratory, yielded comparable values for vertical precision (0.1–0.4 m) (Kirk and others, 2011). Pixel matching error is influenced by signal-to-noise ratio, scene contrast, and differences in illumination between images. Also, pattern noise in the DEM can be introduced by the automatic terrain extraction algorithm, especially in areas of low correlation (for example, on smooth, low-contrast slopes and along shadow edges).

Mapping was completed exclusively within the areal extent of each DEM; the region of stereo overlap in the HiRISE data defined the extent of each map area. The 1 m/pixel orthorectified HiRISE images served as the mapping base and were most useful for identifying the mapped features (for example, layers, faults, unconformities); the 0.25 m/pixel versions were used only to verify meter-scale features such as bedforms and fault offsets that were initially interpreted by using the 1 m/pixel images. The 1 m/pixel images have the advantage of being

Table 1. HiRISE and CTX data used for the eastern Candor Sulci map, western Ceti Mensa map, and southeastern Ceti Mensa map.

Observation ID	Instrument	Description
Eastern Candor Sulci map		
ESP_024967_1755	HiRISE	Map base; stereopair with ESP_024822_1755
ESP_024822_1755	HiRISE	Map base; stereopair with ESP_024967_1755
ESP_035015_1755	HiRISE	Non-stereo
ESP_027644_1750	HiRISE	Stereopair with ESP_027288_1750
ESP_027288_1750	HiRISE	Stereopair with ESP_027644_1750
ESP_024255_1750	HiRISE	Stereopair with ESP_024110_1750
ESP_024110_1750	HiRISE	Stereopair with ESP_024255_1750
ESP_020075_1750	HiRISE	Stereopair with ESP_019719_1750
ESP_019719_1750	HiRISE	Stereopair with ESP_020075_1750
PSP_006164_1750	HiRISE	Non-stereo
D12_031824_1730_XN_07S076W	CTX	Stereopair with D12_031758_1730_XN_07S076W
D12_031758_1730_XN_07S076W	CTX	Stereopair with D12_031824_1730_XN_07S076W
G17_024967_1755_XN_04S076W	CTX	Stereopair with G17_024822_1755_XI_04S076W
G17_024822_1755_XI_04S076W	CTX	Stereopair with G17_024967_1755_XN_04S076W
G10_022066_1739_XI_06S076W	CTX	Stereopair with G09_021631_1739_XI_06S076W
G09_021631_1739_XI_06S076W	CTX	Stereopair with G10_022066_1739_XI_06S076W
P07_003896_1743_XI_05S076W	CTX	Stereopair with P05_002841_1744_XI_05S076W
P05_002841_1744_XI_05S076W	CTX	Stereopair with P07_003896_1743_XI_05S076W
Western Ceti Mensa map		
PSP_003896_1740	HiRISE	Map base; stereopair with PSP_002841_1740
PSP_002841_1740	HiRISE	Map base; stereopair with PSP_003896_1740
ESP_035582_1745	HiRISE	Non-stereo
ESP_035305_1740	HiRISE	Stereopair with ESP_034804_1740
ESP_034804_1740	HiRISE	Stereopair with ESP_035305_1740
ESP_031824_1740	HiRISE	Stereopair with ESP_031758_1740
ESP_031758_1740	HiRISE	Stereopair with ESP_031824_1740
ESP_016317_1740	HiRISE	Stereopair with PSP_008814_1740
ESP_015895_1745	HiRISE	Stereopair with ESP_011794_1745
ESP_013350_1745	HiRISE	Non-stereo
ESP_011794_1745	HiRISE	Stereopair with ESP_015895_1745
PSP_008814_1740	HiRISE	Stereopair with ESP_016317_1740
PSP_007232_1740	HiRISE	Stereopair with PSP_007021_1740
PSP_007021_1740	HiRISE	Stereopair with PSP_007232_1740
PSP_003329_1745	HiRISE	Non-stereo
PSP_002907_1745	HiRISE	Non-stereo
D12_031824_1730_XN_07S076W	CTX	Stereopair with D12_031758_1730_XN_07S076W
D12_031758_1730_XN_07S076W	CTX	Stereopair with D12_031824_1730_XN_07S076W
G10_022066_1739_XI_06S076W	CTX	Stereopair with G09_021631_1739_XI_06S076W
G09_021631_1739_XI_06S076W	CTX	Stereopair with G10_022066_1739_XI_06S076W
B02_010515_1742_XN_05S075W	CTX	Stereopair with B01_009882_1743_XN_05S075W
B01_009882_1743_XN_05S075W	CTX	Stereopair with B02_010515_1742_XN_05S075W
P07_003896_1743_XI_05S076W	CTX	Stereopair with P05_002841_1744_XI_05S076W
P05_002841_1744_XI_05S076W	CTX	Stereopair with P07_003896_1743_XI_05S076W
P03_002063_1733_XI_06S075W	CTX	Non-stereo

Table 1. HiRISE and CTX data used for the eastern Candor Sulci map, western Ceti Mensa map, and southeastern Ceti Mensa map.—Continued

Observation ID	Instrument	Description
Southeastern Ceti Mensa map		
ESP_012295_1730	HiRISE	Map base; stereopair with ESP_011372_1730
ESP_011372_1730	HiRISE	Map base; stereopair with ESP_012295_1730
ESP_029767_1735	HiRISE	Non-stereo
ESP_028422_1730	HiRISE	Stereopair with ESP_026378_1730
ESP_028277_1735	HiRISE	Stereopair with ESP_028211_1735
ESP_028211_1735	HiRISE	Stereopair with ESP_028277_1735
ESP_027578_1730	HiRISE	Non-stereo
ESP_026523_1735	HiRISE	Stereopair with ESP_025600_1735
ESP_026378_1730	HiRISE	Stereopair with ESP_028422_1730
ESP_025600_1735	HiRISE	Stereopair with ESP_026523_1735
ESP_023622_1730	HiRISE	Non-stereo
ESP_017174_1730	HiRISE	Non-stereo
PSP_009671_1725	HiRISE	Non-stereo
PSP_008168_1730	HiRISE	Non-stereo
PSP_002063_1735	HiRISE	Map base for Okubo (2014); stereopair with PSP_001641_1735
PSP_001641_1735	HiRISE	Map base for Okubo (2014); stereopair with PSP_002063_1735
B02_010515_1742_XN_05S075W	CTX	Stereopair with B01_009882_1743_XN_05S075W
B01_009882_1743_XN_05S075W	CTX	Stereopair with B02_010515_1742_XN_05S075W
P03_002063_1733_XI_06S075W	CTX	Stereopair with P02_001641_1734_XI_06S075W
P02_001641_1734_XI_06S075W	CTX	Stereopair with P03_002063_1733_XI_06S075W

8 percent of the file size of the 0.25 m/pixel versions (more efficient file compression and a smaller volume of data to start with), and thus, require significantly less system resources to display onscreen. Both halves of the HiRISE stereopair were used for mapping, because their slightly different illumination geometry aided with distinguishing between meter-scale albedo and topographic variability. Additionally, map-projected HiRISE color products, where available, were valuable for distinguishing between albedo variations and topography.

Structural attitude measurements were aided and verified by using anaglyphs constructed from the HiRISE images as well as three-dimensional perspective views generated by overlaying the orthorectified images onto the corresponding DEM. Anaglyphs were manipulated (stretched, rescaled) using Adobe Photoshop CS5 software and perspective views were constructed using ENVI 4.8 software. The HiRISE anaglyphs provided quick map-view visualizations of dip directions while the three-dimensional perspective views were most useful for examining orientations and crosscutting relations that were ambiguous in map view. Also, these perspective views helped in locating the outcrops that were best suited for measuring structural orientations (that is, those outcrops that most clearly exposed the structures' three dimensions) and in verifying the general magnitude of dip and dip direction of the resulting measurement. Shaded-relief images were constructed from the DEM with the intent of using them to help verify general structural trends in the map area; however, these images were not helpful because the topographic edges of the features of interest could not be clearly discerned from the surrounding outcrop.

Interpretations of stratigraphic relations and structure within each map area were checked for consistency with local strata in surrounding, unmapped areas by using adjacent HiRISE and Mars Reconnaissance Orbiter (MRO) CTX (Malin and others, 2007) images and anaglyphs. The HiRISE observations served as the primary data for these consistency checks, while the CTX observations were used to link interpretations made in adjacent, but nonoverlapping, HiRISE images. HiRISE- and CTX-coordinated observations (for example, Zurek and Smrekar, 2007) were used when possible to maintain consistent lighting and viewing geometries between datasets. The CTX data were processed using the U.S. Geological Survey's Integrated Software for Imagers and Spectrometers. Table 1 lists the HiRISE and CTX observations that were employed during construction of the southeastern Ceti Mensa, western Ceti Mensa, and eastern Candor Sulci maps, respectively. Compact Reconnaissance Imaging Spectrometer for Mars (CRISM) multispectral summary products (Pelkey and others, 2007; Murchie and others, 2009b) of each map area were assessed for their potential in correlating units on a regional scale but were ultimately not used because of their limited areal coverage and low spatial resolution.

Methodology

All mapping was conducted by using the ArcMap 10.2 geographic information system (GIS) software package with custom plug-ins. A separate ArcMap project was set up for each map area, and the corresponding HiRISE DEMs and orthorectified images were imported into each project. Because the orthorectified images were processed using their corresponding DEM, no further coregistration was required in ArcMap. Each DEM was imported as a 32-bit floating point tagged image file format (TIFF) image, and the orthorectified images were imported in 8-bit unsigned integer JPEG2000 format. Features were point digitized at 1:4,000 to 1:6,000 scale. Linear features with a length of less than 50 m and area features less than 20 m in maximum extent were not mapped.

All measurements of structural orientation (strike and dip) were made using the Layer Tools plug-in for ArcMap (Kneissl and others, 2010). Layer Tools referenced the HiRISE DEM and orthorectified images linked to each project to calculate the orientations of discontinuities (layer bounding surfaces, regional unconformities, faults). Orientations were defined by first measuring northing, easting, and elevation triplets at five points along the trace of each discontinuity from the DEM. These five points were roughly evenly spaced along a 50–100 m chord length along the discontinuity. A best-fit plane was then calculated for the five points, and the orientation of this plane was used to define the strike and dip of the discontinuity. This technique is similar in concept to a classic three-point problem but is less susceptible to noise in the DEM and the discontinuities' actual deviation from planarity at length-scales of 10 to 100 m. This was the same process employed to perform similar HiRISE-based structural measurements elsewhere in western Candor Chasma (for example, Okubo and others, 2008; Okubo 2010, 2014). Potential sources of error for these measurements include inaccuracies in the HiRISE DEM, especially in areas where stereo correlation tends to be poor (for example, smooth, low-contrast slopes and along shadow edges); misinterpretation of discontinuities; and nonplanar discontinuities at 50- to 100-m-length scales. Measurements were not taken in areas of potentially low stereo correlation, when recognized in the orthorectified images.

Orientation measurements with root mean square deviations (RMSD) of less than 1 m were used in the construction of these maps. Measurements associated with larger values of RMSD were discarded. RMSD values were stored as ancillary data to each measurement in the supplementary GIS databases that accompany the online version of this report. Assuming ±2 m residuals across a linear distance of 75 m (the median chord length for the orientation measurements) yields an order of magnitude estimate of 3° uncertainty in the magnitude of the best-fit dip.

Previous geologic mapping in these three map areas defined units largely on the basis of geomorphology (for example, Scott and Tanaka, 1986; Witbeck and others, 1991). This approach was not strictly adopted here because the geomorphology of the sedimentary units does not always vary significantly at the scale of these maps. In these maps, all units are allostratigraphic; that is, they are defined by unconformities at their upper and lower contacts. An allostratigraphic approach was selected because, at HiRISE scale, bounding unconformities can be directly observed, are the most prominent stratigraphic divisions observed, and are mappable in a systematic way. Once identified in HiRISE data, these unconformities can often be traced over multiple kilometers in CTX images.

Various types of unconformities are recognized. Angular unconformities are observed where underlying layers are truncated by a common irregular surface and are buried by subsequent layers that have a recognizably different orientation. Disconformities are observed where underlying layers are truncated by a common irregular surface, and subsequent layers are subparallel to older layers. Paraconformities are observed where an unconformity parallels a distinct layer surface that is bounded by adjacent layers that have similar attitudes. Paraconformities are interpreted as surfaces that result from erosion or nondeposition that parallel existing layers and are later buried by sediments that parallel older strata.

Though there are numerous unconformities in the mapped sedimentary units, not all unconformities define unique geologic units. Instead, geologic units are primarily defined by the most areally extensive unconformities observed within the map area and in adjacent terrain. Secondarily, each geologic unit is described using characteristic surface expressions (albedo, erosional texture, bedforms). Each unit may contain numerous subordinate unconformities that do not define unit boundaries. The intent of this approach is to define broad units that are mappable at regional scales to facilitate future efforts to correlate units between these and other high-resolution geologic maps. Mapping focused on sedimentary bedrock and volcanic wall rock and sediments derived from the wall rock. Surficial materials such as eolian sand dunes and impact crater ejecta were not mapped here as distinct units.

Unit names are based on their morphology and reference their geographic occurrence where appropriate (table 2). Unit labels are abbreviated unit names. Geographic features are abbreviated using uppercase letters, followed by any lowercase letters that are required for uniqueness among regional feature names. Cardinal directions are abbreviated in uppercase initials and appended as a subscript to geographic abbreviations where appropriate. Additionally, morphologic descriptions are abbreviated in lowercase letters and appended as a subscript as needed. The Ceti Mensa southeast blocky unit is abbreviated as $\mathrm{CeM}_{\mathrm{SEb}}$, with "CeM" being an abbreviation for Ceti Mensa (the "e" being necessary to distinguish it from a possible future abbreviation of Candor Mensa). The subscript "$_{\mathrm{SE}}$" indicates that the unit is located on the southeast flank of Ceti Mensa, and the "$_{\mathrm{b}}$" is an abbreviation for its blocky morphology. Units that have no apparently meaningful geographic designation are given unit labels with only morphologic descriptions abbreviated in lowercase letters. For example, materials similar in morphology to the chasma footwall unit occur throughout Valles Marineris; therefore, the unit is given a label, "cf", which is not specific to any one geographic feature. This naming convention is consistent with, and complementary to, that of Okubo (2014). In cases where mapping covers a unit previously identified by Okubo (2014), the unit name, label, and color of Okubo (2014) are used. Though previous mapping efforts incorporated

chronostratigraphic designations in their unit labels (for example, Scott and Tanaka, 1986; Witbeck and others, 1991), such designations have been set aside in these maps until more of this region can be mapped at higher resolution and the regional stratigraphy can be reassessed.

The level of confidence in the position of surface traces for fractures and unconformities is classified as accurate, approximate, or concealed. Additionally, a 1-m zone of confidence is adopted and extends 1 m on either side of the mapped feature. The location of a surface trace is considered accurate where the feature is fully exposed (not partially or completely buried by surficial materials); its plotted position on the map is within the zone of confidence. An approximate trace is one where the feature is known to exist due to well-defined exposures elsewhere, but where the trace cannot be precisely located. Its plotted position may not be within the zone of confidence. Approximate traces are often mapped where features cannot be distinguished from adjacent subparallel features at the resolution limit of the HiRISE images, or in areas where there is a low contrast in albedo between the surface trace and surrounding materials. A concealed trace is one where the feature is known to exist on the basis of well-defined exposures elsewhere or interpreted formation mechanisms, but the trace cannot be directly observed due to cover of surficial sediments or superposed units. The position of a concealed feature may not be within the zone of confidence. Concealed features have the lowest level of confidence in their assigned locations.

All unconformities have a high level of confidence in their identity. Only unconformities that are clearly identifiable in HiRISE images are mapped. Depositional discontinuities, including angular unconformities, disconformities, paraconformities, and nonconformities, are mapped as unconformities. Paraconformities are mapped only where the discontinuity can be traced laterally to a different type of unconformity.

For faults, the level of confidence in the identity of fractures is indicated by the specificity of their classification. Classifications of "normal fault" and "thrust fault" are given where the strike and dip of the fault plane are clear and sense of displacement along the fault is evident based on crosscutting relations. The generic "fracture" classification is given where a structural discontinuity is observed, but either the fault geometry, sense of displacement, or both cannot be determined with certainty.

Age Determinations

The Noachian sedimentary, impact, and volcanic materials exposed along the walls of western Candor Chasma and the Hesperian sedimentary units exposed within the chasma (Tanaka, 2014) are investigated in this set of three maps. New ages based on crater counts were not acquired because these sedimentary units likely consist of sulfate-rich sands similar to those found in Meridiani Planum (Murchie and others, 2009a), and the standard techniques for relative age dating based on impact crater retention cannot be relied upon in these highly friable deposits. In this work, relative ages of geologic units are based solely upon superposition and crosscutting relations.

Table 2. Unit stratigraphic relations, western Ceti Mensa, southeastern Ceti Mensa, and eastern Candor Sulci regions of Mars.

Unit label	Aerial extent (km^2)	Relative age
	Western Ceti Mensa	
CeM_{Wu}	36.85	Younger than all other units
CeM_{Wm}	32.52	Younger than unit CeM_{Wh}; older than unit CeM_{Wu}
CeM_{Wh}	4.37	Older than all other units
	Southeastern Ceti Mensa	
cf	0.98	Long-lived unit; deposition predates, is contemporaneous with, and postdates, all other units; most recently active
CeM_{SEb}	53.73	Younger than units CaC, NiT_{l4}, NiT_{l3}, NiT_{l2}, and NiT_{l1}
CaC	1.10	Younger than units NiT_{l4}, NiT_{l3}, NiT_{l2}, and NiT_{l1}; older than unit CeM_{SEb}
NiT_{l4}	1.85	Younger than units NiT_{l3}, NiT_{l2}, and NiT_{l1}; older than units CeM_{SEb} and CaC
NiT_{l3}	8.57	Younger than units NiT_{l2} and NiT_{l1}; older than units CeM_{SEb}, CaC, and NiT_{l4}
NiT_{l2}	27.74	Younger than unit NiT_{l1}; older than units CeM_{SEb}, CaC, NiT_{l4}, and NiT_{l3}
NiT_{l1}	7.38	Older than units CeMSEb, CaC, NiT_{l4}, NiT_{l3}, and NiT_{l2}
	Eastern Candor Sulci	
cf	45.41	Long-lived unit; deposition predates, is contemporaneous with, and postdates, all other units; most recently active
CaS	38.47	Younger than units CaL and cwr
CaL	3.43	Younger than unit cwr; older than unit CaS
cwr	5.42	Older than all other units

Geologic History

In this section, separate geologic histories are presented for each map area. Then, in a concluding subsection, a regional geologic history for western Candor Chasma is given based on the results of these three maps plus the works of Okubo and others (2008) and Okubo (2010, 2014). Stratigraphic correlations between these disparate map areas are made using CTX images.

Eastern Candor Sulci

In the eastern Candor Sulci map area (figs. 1, 2), the chasma wall rock unit (cwr) was deposited as successions of sedimentary, impact, and volcanic materials during the

Noachian (Tanaka, 2014). Candor Chasma and other troughs of Valles Marineris began to form in the Late Noachian and continued into the Early Hesperian (Tanaka, 2014). Unit cwr was exposed along the walls of western Candor Chasma, and the chasma foothill unit (cf) began to accumulate as colluvium shed from unit cwr. The Candor Labes unit (CaL) formed through slope failure and landsliding of unit cwr. The Candor Sulci unit (CaS) was then deposited. Unit CaS buried a ridge composed of units cwr and cf in the central part of the map area, as well as unit CaL (figs. 3, 4; table 2).

We interpret the deposition of unit CaS to have occurred in a low-energy environment because of the apparent preservation of the underlying unit cf materials (fig. 4). Unit cf is interpreted to be poorly lithified on the basis of large amounts of colluvium (boulders, cobbles, and possibly sand) that have shed from this unit onto topographically lower exposures of units CaS and cwr, as well as occasional boulder tracks observed within unit cf. Unit cf materials are typically observed on topographic highs and along steep slopes; therefore, deposition of unit CaS required a sufficiently low-energy environment so that the unit cf materials remained largely in place. Further, neither fluvial nor shore-zone erosional features or deposits are observed in the map area. On the basis of these findings, sedimentation is interpreted to have occurred in a subaerial environment.

Unit CaS eventually experienced slope failure and landsliding. The breccia facies of unit CaS is interpreted to be comminuted unit CaS material along the basal shear zone of this landslide. The landslide moved in a northerly direction, which is downslope from portions of unit CaS located at higher elevations to the south. Translation of this slide involved unit CaS material on both sides of the central ridge of unit cwr. The slide appears to have broken into large blocks as it passed over this ridge. The morphology of this landslide is consistent with a translational slide—the downslope movement of material along a planar to gently undulating zone of weakness (for example, Varnes, 1978). The triggering mechanism for this landslide has not been determined.

Unit CaS displays planar, low-angle, and wavy stratification, with individual layers being 1–3 m thick. Mean dip angle of the layers is 25±17°, and dip directions are predominantly toward the south (fig. 5). Primary depositional stratification is not clear because all exposures of this unit within the map area have been affected by landslide-related deformation. Therefore, the provenance of these sediments is not clear beyond being subaerially deposited.

Aside from unit CaS, no other stratified sedimentary units are in the map area. Unit CaS may have been the last stratified sedimentary unit deposited in this area, or subsequent units have been completely eroded away. Following deposition of the last stratified sedimentary unit in this area, the sediments experienced deflation through eolian erosion. This deflation removed the upper portions of the landslide in unit CaS and exposed its basal shear zone (breccia facies). This process of deflation, as well as development of unit cf along the chasma walls, has continued into the present.

Southeastern Ceti Mensa

In the southeastern Ceti Mensa map area (figs. 1, 2), Candor Chasma began to form in the Late Noachian and continued into the Early Hesperian (Tanaka, 2014). The chasma foothill unit (cf) accumulated as colluvium shed from rock exposed along the walls of the developing chasma. No outcrops of chasma wall rock are observed in the map area; they are inferred to underlie unit cf. Outcrops of chasma wall rock may be in the map area, but they cannot be clearly distinguished from the autochthonous unit cf.

The four lowest, layered sedimentary units in the map area are the Nia Tholus lower 1 through 4 units (table 2; fig. 6). The name of these units references Nia Tholus, the summit of which is located immediately east of the map area; this map area straddles the boundary between Ceti Mensa and Nia Tholus. The lowest of these units, the Nia Tholus lower 1 unit (NiT_{l1}), is exposed within the central parts of small knobs, along the tops of ridges, and along slope faces in the southern end of the map area.

Unit NiT_{l1} accumulated on top of unit cf and blanketed the preexisting chasma topography. Then, unit NiT_{l1} experienced a period of deep erosion, which exposed its lower contact with unit cf. Unit NiT_{l2} subsequently buried units cf and NiT_{l1}. Deposition of unit NiT_{l2} ceased, and this unit experienced another period of erosion. In places, unit NiT_{l2} has been reduced to a veneer, and the morphology of the underlying layers of unit NiT_{l1} is apparent. Units NiT_{l3} and NiT_{l4} were then deposited, with an interval of erosion separating the two units and following deposition of unit NiT_{l4}. Given that unit cf is interpreted as a colluvial deposit, it would have been continually shed from the chasma wall rock during deposition of the Nia Tholus units. The intercalation of units cf, NiT_{l1}, and NiT_{l2}, and evidence of present-day reworking of unit cf is demonstrated at the top and along the flanks of a knob in the southeast part of the map area (fig. 7).

Deposition and erosion of the sedimentary units is interpreted to have occurred in a low-energy environment because of the apparent preservation of the underlying unit cf materials. Unit cf is interpreted to be poorly lithified and actively modified by gravity-driven processes on the basis of the large amounts of colluvium (boulders, cobbles, and possibly sand) that have shed from this unit onto topographically lower exposures of stratigraphically younger units NiT_{l1} and NiT_{l2} (fig. 7), as well as on the basis of occasional boulder tracks observed within unit cf. Unit cf materials are typically observed on topographic highs and along steep slopes; therefore, deposition and erosion of units NiT_{l1}, NiT_{l2}, and superposed units required a sufficiently low-energy environment so that unit cf materials remained largely in place. Further, no fluvial or shore-zone erosional features or deposits are observed. The erosional surfaces that bound the Nia Tholus units are areally extensive and have long-wavelength relief. On the basis of these findings, sedimentation is interpreted to have occurred in a subaerial environment. The regional erosional surfaces would have thus formed through eolian deflation and are analogous to supersurfaces (inter-erg

bounding surfaces; see, for example, Kocurek, 1988) in terrestrial sedimentary sequences.

Sediments within the Nia Tholus units are planar to low-angle stratified and have layers that are 1–5 m thick. The layers contain discontinuous bedding that is subparallel to their bounding surfaces. Trough cross-stratification and crossbedding, as resolved in the HiRISE data, are rare.

Considering all four Nia Tholus lower units together, the mean dip angle of the layers is 14±8°, predominantly in a northerly direction (fig. 8). Dips are steepest in the southernmost part of the map area within units NiT_{l1} and NiT_{l2} and become shallower toward the north. Individual layers can be traced laterally for as many as 5 km within the map area, with some layers traceable beyond the map boundaries. The planar to low-angle stratification of the layers, the discontinuous and subparallel bedding within the layers, and the inferred subaerial depositional environment suggest that these sediments are eolian sand sheets (for example, Fryberger and others, 1979; Loope, 1984).

Following deposition of the Nia Tholus units, sedimentation continued and led to development of the Candor Colles unit (CaC). Unit CaC is planar to low-angle stratified and has layers that are 1–2 m thick. The layers contain discontinuous bedding that is subparallel to bounding surfaces. HiRISE images do not show evidence of either trough cross-stratification or crossbedding. Accordingly, unit CaC is interpreted to consist of eolian sand sheets. Mean dip angle of the layers is 11±6°, with southerly dip directions being prevalent (fig. 8). These orientations suggest that sediments of unit CaC bury southerly facing slopes of a preexisting sediment mound, essentially the nascent Ceti Mensa. After deposition of unit CaC, sedimentation continued with the deposition of stratigraphically higher sedimentary rocks on Ceti Mensa.

Stratified sedimentary rocks above unit CaC, at higher elevations on Ceti Mensa, eventually became unstable and failed, forming a large landslide. This landslide came to rest within the topographic low, or moat, between Ceti Mensa and the south wall of western Candor Chasma. This landslide deposit is delineated as unit CeM_{SEb} in the map area. We interpret the breccia facies of unit CeM_{SEb} to consist of comminuted fragments of the failed sedimentary rocks. The morphology of this landslide resembles that of a translational slide, which involves the failure of material along a planar to gently undulating zone of weakness (for example, bedding planes) that dips downslope (Varnes, 1978). This landslide may have been triggered by oversteepening of the slopes of Ceti Mensa due to erosion, a rise in the groundwater table, or seismic shaking from slip along a nearby fault or an impact event. Unit CeM_{SEb} exhibits little to no relief above the underlying Nia Tholus units (fig. 2), indicating that this landslide experienced significant deflation after emplacement. Individual layers within intact blocks of unit CeM_{SEb} are 1–2 m thick and have subparallel to wavy stratification, which may result from primary deposition or subsequent deformation.

Deposition of sedimentary units eventually ceased completely in this area. These units were subsequently modified by eolian deflation, and unit cf has continued to develop along the chasma walls into the present.

Western Ceti Mensa

In the western Ceti Mensa map area (figs. 1, 2), the Ceti Mensa west hummocky unit (CeM_{Wh}) was deposited on top of older sediments that constitute the lower portions of Ceti Mensa. Following deposition, unit CeM_{Wh} experienced slope failure and landsliding, resulting in the formation of its characteristic elongated knobs and ridges. Each knob is a block within the landslide, and the ridges are interpreted as pressure ridges within the toe region of the slide. The morphology of this landslide is consistent with a lateral spread, which involves movement of material along subhorizontal planes of weakness such as bedding (Varnes, 1978). Lateral spreads form through liquefaction (Varnes, 1978), suggesting that unit CeM_{Wh} was poorly consolidated and water saturated at the time of failure. The triggering mechanism for this landslide has not been determined.

Unit CeM_{Wh} is massive, with only a few poorly defined layers discernable. If this unit had deformed through lateral spreading as proposed here, the lack of layering could be attributed to soft-sediment deformation attendant with the spread. Alternatively, this unit may have had a massive primary texture, or bedding may be too thin to be resolved.

Following landsliding of unit CeM_{Wh}, the Ceti Mensa west mottled unit (CeM_{Wm}) (table 2; figs. 9, 10) buried the landslide blocks of unit CeM_{Wh}. Deposition of unit CeM_{Wm} eventually ceased and the region experienced a period of widespread erosion that cut through unit CeM_{Wm} and exposed the underlying landslide blocks of unit CeM_{Wh}. The Ceti Mensa west upper unit (CeM_{Wu}) was then deposited on the deflation surface at the top of unit CeM_{Wm}. Unit CeM_{Wu} is the highest allostratigraphic unit preserved on Ceti Mensa and may have been one of the last sedimentary units deposited in this part of western Candor Chasma. Following deposition of unit CeM_{Wu}, regional erosion exposed the underlying units CeM_{Wh} and CeM_{Wm}. Eolian erosion has continued to modify these units into the present.

The erosional surface at the top of unit CeM_{Wm} is areally extensive and has long-wavelength relief. Neither fluvial nor shore-zone erosional features or deposits are observed on this surface. On the basis of this morphology, the erosional surface is interpreted to have formed through eolian deflation, analogous to supersurfaces (Kocurek, 1988) in terrestrial sedimentary sequences. Accordingly, units CeM_{Wm} and CeM_{Wu} are interpreted as subaerially deposited sediments. Observations of unit CeM_{Wh} in the map area do not provide clear constraints on its depositional setting.

Units CeM_{Wm} and CeM_{Wu} are planar to trough cross-stratified. Individual layers are 1–2 m thick and have discontinuous bedding that is subparallel to nonparallel with their bounding surfaces. Individual layers can be traced laterally as far as 4 km in both units. Mean dip angle of the layers in both units is 8±7°,

with no predominant dip direction (fig. 11). Given this pattern of stratification and the inferred subaerial depositional environment, these units are interpreted to be composed of eolian sand sheets and sand dunes.

Regional History

The chasma wall rock unit (cwr) was deposited as successions of sedimentary, impact, and volcanic materials during the Noachian (Tanaka, 2014). Candor Chasma and other troughs of Valles Marineris began to form in the Late Noachian and continued into the Early Hesperian (Tanaka, 2014). Unit cwr was exposed along the walls of western Candor Chasma. The chasma foothill unit (cf) began to accumulate as colluvium shed from unit cwr and continued to develop in this way throughout the geologic history of western Candor Chasma.

On the north side of western Candor Chasma (eastern Candor Sulci map area), portions of unit cwr became unstable and failed, resulting in the formation of the Candor Labes landslide (unit CaL). This landslide came to rest on the floor of western Candor Chasma. The Candor Sulci unit (CaS) was then deposited on top of unit CaL. Subsequently, unit CaS also became unstable and failed. The resulting landslide displaced unit CaS material toward the north.

Because unit CaS buries unit cwr and the mass-wasting deposits derived from it, the stratigraphic position of unit CaS appears to be comparable to the Nia Tholus lower units on the south side of the chasma. The exact stratigraphic relation of unit CaS to other mapped stratified sedimentary units has not been determined, however, because stratigraphic relations in the region between the eastern Candor Sulci map area and the other geologic map areas discussed here are not clear in existing HiRISE and CTX images.

On the south wall of western Candor Chasma (southeastern Ceti Mensa map area), the Nia Tholus lower 1 unit (NiT_{l1}) accumulated on top of units cwr and cf. Deposition of unit NiT_{l1} eventually ceased and the unit was eroded by eolian deflation. Subsequently, the Nia Tholus lower 2 unit (NiT_{l2}) was deposited on the deflation surface at the top of unit NiT_{l1}. Deposition of the Nia Tholus lower 3 and 4 units (NiT_{l3} and NiT_{l4}) followed, with periods of regional eolian deflation occurring after each unit was deposited.

All four Nia Tholus lower units consist of eolian sand sheets, which recorded the start of extensive erg development within western Candor Chasma. Regional unconformities bounding each unit are interpreted as supersurfaces. Supersurfaces can develop within an erg due to changes in climate, base level, water table depth, tectonic setting, or erg migration (Kocurek, 1988). The specific mechanisms of formation for the supersurfaces observed in western Candor Chasma were not determined.

Following deposition of the Nia Tholus units, eolian sand sheets continued accumulating, leading to deposition of the Candor Colles unit (CaC). Unit CaC reflects the nascent topography of Ceti Mensa, and growth of Ceti Mensa must have begun during deposition of the Nia Tholus units or earlier.

Near the end of unit CaC deposition, the southern slope of Ceti Mensa became unstable, leading to the development of landslides that displaced the sediments toward the south. Though these landslides developed mainly within unit CaC, the Nia Tholus units were affected to a lesser degree. These landslides drove soft-sediment deformation, principally contorted layering and injectite megapipes, within unit CaC (Okubo, 2014). The development of soft-sediment deformation, especially the injectites, supports the interpretation that these sediments are clastic and also indicates that these sediments were poorly indurated and water-saturated at the time of deformation (for example, Chan and others, 2007). Therefore, the extant geologic setting can be further described as an eolian-dominated wet playa. The landslides may have been triggered by oversteepening of the slopes of Ceti Mensa due to erosion, a rise in the groundwater table, or seismic shaking from slip along a nearby fault or an impact event.

Following landsliding on the southern slope of Ceti Mensa, the region experienced another period of eolian deflation. This was followed by continued cycles of sedimentation and periodic eolian deflation.

Sedimentary rocks above unit CaC, at higher elevations on Ceti Mensa, eventually became unstable and failed, forming another large landslide. This landslide came to rest within the moat between Ceti Mensa and the south wall of the chasma. This landslide deposit is delineated as the Ceti Mensa southeast blocky unit (CeM_{SEb}) in the southeastern Ceti Mensa map area.

Another slope failure occurred near the summit of Ceti Mensa, in the Ceti Mensa west hummocky unit (CeM_{Wh}), which is at a stratigraphic interval similar to the source rocks of the unit CeM_{SEb} landslide (fig. 9). The morphology of this landslide is consistent with a lateral spread, which typically forms through liquefaction (Varnes, 1978), suggesting that unit CeM_{Wh} was poorly consolidated and water saturated at the time of failure. The massive bedding observed in unit CeM_{Wh} could have developed during this process of liquefaction (for example, Chan and others, 2007), although massive primary bedding cannot be ruled out. Given the subaerial depositional setting of the adjacent older and younger stratified sediments, unit CeM_{Wh} was likely deposited subaerially.

Following the landsliding of unit CeM_{Wh}, the Ceti Mensa west mottled unit (CeM_{Wm}) formed as a result of renewed accumulation of eolian sand sheets and sand dunes. Following deposition of unit CeM_{Wm}, the region experienced another period of eolian deflation. The Ceti Mensa west upper unit (CeM_{Wu}) was then deposited on top of this deflation surface as accumulations of eolian sand sheets and sand dunes.

The presence of sand dunes in units CeM_{Wm} and CeM_{Wu} suggests a change in depositional environment from that of the older stratified units CaC and the Nia Tholus lower units, which largely consist of sand sheets. Formation of sand sheets is favored over sand dunes where (1) the groundwater table is high, (2) sediment moisture content is high, and (3) sediments are rapidly cemented (for example, Loope, 1984; Kocurek and

Nielson, 1986). Therefore, the onset of dune formation within units CeM_{Wm} and CeM_{Wu} signals a shift toward an increasingly arid depositional environment.

Deposition of stratified sedimentary deposits in western Candor Chasma eventually ceased near the end of the Hesperian (Tanaka, 2014). Eolian activity, accompanied by occasional impact cratering and development of unit cf, became the dominant geologic processes and have continued into the present.

References Cited

Batson, R.M., Bridges, P.M., and Inge, J.L., 1979, Atlas of Mars, the 1:5,000,000 map series: National Aeronautics and Space Administration Special Publication 438, 146 p.

Birnie, C., Fueten, F., Stesky, R.M., and Hauber, E., 2012, Underlying structural control of small-scale faults and fractures in West Candor Chasma, Mars: Journal of Geophysical Research, v. 117, no. E11, p. E11001.

Bridges, P.M., and Inge, J.L., 1972, Shaded relief map of Mars—Atlas of Mars: U.S. Geological Survey Miscellaneous Investigations Series Map I-810, scale 1:25,000,000.

Catling, D.C., Wood, S.E., Leovy, C., and 4 others, 2006, Light-toned layered deposits in Juventae Chasma, Mars: Icarus, v. 181, no. 1, p. 26–51.

Chan, M.A., Netoff, D.I., Blakey, R.C., Kocurek, G.A., and Alvarez, W., 2007, Clastic-injection pipes and syndepositional deformation structures in Jurassic eolian deposits—Examples from the Colorado Plateau, *in* Hurst, A., and Cartwright, J., eds., Sand injectites—Implications for hydrocarbon exploration and production: American Association of Petroleum Geologists Memoir 87, p. 233–244.

Chapman, M.G., and Tanaka, K.L., 2001, Interior trough deposits on Mars—Subice volcanoes?: Journal of Geophysical Research, v. 106, no. E5, p. 10087–10100.

Christensen, P.R., Jakosky, B.M., Kieffer, H.H., and 8 others, 2004, The Thermal Emission Imaging System (THEMIS) for the Mars 2001 Odyssey Mission, *in* Russell, C., ed., 2001 Mars Odyssey: Dordrecht, Netherlands, Kluwer Academic Publishers, p. 85–130.

Dromart, G., Quantin, C., and Broucke, O., 2007, Stratigraphic architectures spotted in southern Melas Chasma, Valles Marineris, Mars: Geology, v. 35, no. 4, p. 363–366.

Flahaut, J., Mustard, J.F., Quantin, C., and 3 others, 2011, Dikes of distinct composition intruded into Noachian–aged crust exposed in the walls of Valles Marineris: Geophysical Research Letters, v. 38, no. 15, 7p.

Flahaut, J., Quantin, C., Clenet, H., and 3 others, 2012, Pristine Noachian crust and key geologic transitions in the lower walls of Valles Marineris—Insights into early igneous processes on Mars: Icarus, v. 221, no. 1, p. 420–435.

Fryberger, S.G., Ahlbrandt, T.S., and Andrews, Sarah, 1979, Origin, sedimentary features, and significance of low-angle eolian "sand sheet" deposits, Great Sand Dunes National Monument and vicinity, Colorado: Journal of Sedimentary Research, v. 49, no. 3, p. 733–746.

Fueten, F., Stesky, R.M., MacKinnon, P., and 5 others, 2006, A structural study of an interior layered deposit in southwestern Candor Chasma, Valles Marineris, Mars, using high resolution stereo camera data from Mars Express: Geophysical Research Letters, v. 33, no. 7, p. 1–4.

Fueten, F., Stesky, R.M., MacKinnon, P., and 5 others, 2008, Stratigraphy and structure of interior layered deposits in west Candor Chasma, Mars, from High Resolution Stereo Camera (HRSC) stereo imagery and derived elevations: Journal of Geophysical Research, v. 113, no. E10, p. E10008.

Fueten, F., Flahaut, J.D., Stesky, R.M., Hauber, E., and Rossi, A.P., 2014, Stratigraphy and mineralogy of Candor Mensa, West Candor Chasma, Mars—Insights into the geologic history of Valles Marineris: Journal of Geophysical Research, Planets, v. 119, no. 2, p. 331–354.

Jaumann, R., Neukum, G., Behnke, Thomas, and 23 others, 2007, The high-resolution stereo camera (HRSC) experiment on Mars Express—Instrument aspects and experiment conduct from interplanetary cruise through the nominal mission: Planetary and Space Science, v. 55, no. 7, p. 928–952.

Kirk, R.L., Howington-Kraus, A.E., Galuszka, D.M., and 11 others, 2011, Near-complete 1-m topographic models of the MSL candidate landing sites—Site safety and quality evaluation [abs.], *in* European Planetary Science Congress–Division for Planetary Sciences Joint Meeting, Nantes, France, 2011: European Planetary Science Congress, abstract EPSC-DPS2011-1465.

Kirk, R.L., Howington-Kraus, A.E., Rosiek, M.R., and 16 others, 2008, Ultrahigh resolution topographic mapping of Mars with MRO HiRISE stereo images—Meter-scale slopes of candidate Phoenix landing sites: Journal of Geophysical Research, Planets, v. 113, no. E3, p. E00A24.

Kneissl, T., van Gasselt, S., and Neukum, G., 2010, Measurement of strike and dip of geologic layers from remote sensing data—New software tool for ArcGIS [abs.], *in* Lunar and Planetary Science Conference, 41st, The Woodlands, Tex., 2010: Lunar and Planetary Institute, abstract 1540.

Kocurek, G., 1988, First-order and super bounding surfaces in eolian sequences—Bounding surfaces revisited: Sedimentary Geology, v. 56, no. 1–4, p. 193–206.

Kocurek, G., and Nielson, J., 1986, Conditions favourable for the formation of warm-climate aeolian sand sheets: Sedimentology, v. 33, no. 6, p. 795–816.

Loope, D.B., 1984, Eolian origin of upper Paleozoic sandstones, southeastern Utah: Journal of Sedimentary Research, v. 54, no. 2, p. 563–580.

Lucchitta, B.K., 1999, Geologic map of Ophir and central Candor Chasmata (MTM–05072) of Mars: U.S. Geological Survey Geologic Investigations Series I–2568, scale 1:500,000.

Lucchitta, B.K., McEwen, A.S., Clow, G.D., and 4 others, 1992, The canyon system on Mars: Mars, v. 1, p. 453–492.

Malin, M.C., Bell, J.F., III, Cantor, B.A., and 11 others, 2007, Context camera investigation on board the Mars Reconnaissance Orbiter: Journal of Geophysical Research, v. 112, no. E5, p. E05S04.

Malin, M.C., Danielson, G.E., Ingersoll, A.P., and 4 others, 1992, Mars Observer Camera: Journal of Geophysical Research, v. 97, no. E5, p. 7699–7718.

Malin, M.C., and Edgett, K.S., 2003, Evidence for persistent flow and aqueous sedimentation on early Mars: Science, v. 302, no. 5652, p. 1931–1934.

Malin, M.C., and Edgett, K.S., 2001, Mars Global Surveyor Mars Orbiter Camera—Interplanetary cruise through primary mission: Journal of Geophysical Research, Planets, v. 106, no. E10, p. 23429–23570.

Malin, M.C., and Edgett, K.S., 2000, Sedimentary rocks of early Mars: Science, v. 290, no. 5498, p. 1927–1937.

Mangold, N., Gendrin, A., Gondet, B., and 7 others, 2008, Spectral and geological study of the sulfate-rich region of West Candor Chasma, Mars: Icarus, v. 194, no. 2, p. 519–543.

Masursky, H., 1973, An overview of geological results from Mariner 9: Journal of Geophysical Research, v. 78, no. 20, p. 4009–4030.

McCauley, J.F., Carr, M.H., Cutts, J.A., and 5 others, 1972, Preliminary Mariner 9 report on the geology of Mars: Icarus, v. 17, no. 2, p. 289–327.

McCauley, J.F., 1978, Geologic map of the Coprates quadrangle of Mars: U.S. Geological Survey Miscellaneous Investigations Series Map I–897, scale 1:5,000,000.

McEwen, A.S., Banks, M.E., Baugh, N.F., and 67 others, 2010, The high resolution imaging science experiment (HiRISE) during MRO's primary science phase (PSP): Icarus, v. 205, no. 1, p. 2–37.

Metz, J.M., Grotzinger, J.P., Mohrig, D., and 5 others, Sublacustrine depositional fans in southwest Melas Chasma: Journal of Geophysical Research, v. 114, no. E10, p. E10002.

Montgomery, D.R., and Gillespie, A.R., 2005, Formation of Martian outflow channels by catastrophic dewatering of evaporite deposits: Geology, v. 33, no. 8, p. 625–628.

Murchie, S.L., Roach, L.H., Seelos, F.P., and 7 others, 2009a, Evidence for the origin of layered deposits in Candor Chasma, Mars, from mineral composition and hydrologic modeling: Journal of Geophysical Research, v. 114, p. E00D05.

Murchie, S.L., Seelos, F.P., Hash, C.D., and 20 others, 2009b, Compact Reconnaissance Imaging Spectrometer for Mars investigation and data set from the Mars Reconnaissance Orbiter's primary science phase: Journal of Geophysical Research, v. 114, p. E00D07.

Nedell, S.S., Squyres, S.W., and Andersen, D.W., 1987, Origin and evolution of the layered deposits in the Valles Marineris, Mars: Icarus, v. 70, no. 3, p. 409–441.

Okubo, C.H., 2010, Structural geology of Amazonian-aged layered sedimentary deposits in southwest Candor Chasma, Mars: Icarus, v. 207, no. 1, p. 210–225.

Okubo, C.H., 2014, Bedrock geologic and structural map through the western Candor Colles region of Mars: U.S. Geological Survey Scientific Investigations Map 3309, scale 1:18,000.

Okubo, C.H., Lewis, K.W., McEwen, A.S., and Kirk, R.L., 2008, Relative age of interior layered deposits in southwest Candor Chasma based on high-resolution structural mapping: Journal of Geophysical Research, v. 113, no. E12, p. E12002.

Pelkey, S.M., Mustard, J.F., Murchie, S.L., and 9 others, 2007, CRISM multispectral summary products—Parameterizing mineral diversity on Mars from reflectance: Journal of Geophysical Research, v. 112, no. E8, p. E08S14.

Peterson, C., 1982, A secondary origin for the central plateau of Hebes Chasma [abs.]: Lunar and Planetary Science Conference, 12th, Houston, TX, Geochemica et Cosmochemica Acta, p. 1459–1471.

Peulvast, J.P., and Masson, P.L., 1993, Erosion and tectonics in central Valles Marineris (Mars)—A new morpho–structural model: Earth, Moon, and Planets, v. 61, no. 3, p. 191–217.

Schultz, R.A., 1998a, Geologic map of the western Ophir Planum region (MTM–10067) of Mars: U.S. Geological Survey Geologic Investigations Series I–2588–M, scale 1:500,000.

Schultz, R.A., 1998b, Multiple-process origin of Valles Marineris basins and troughs, Mars: Planetary and Space Science, v. 46, no. 6–7, p. 827–834.

Schultz, R.A., and Lin, J., 2001, Three-dimensional normal faulting models of the Valles Marineris, Mars, and geodynamic implications: Journal of Geophysical Research, v. 106, no. B8, p. 16549–16566.

Scott, D.H., and Carr, M.H., 1978, Geologic map of Mars: U.S. Geological Survey Miscellaneous Investigations Series Map I–1083, scale 1:25,000,000.

Scott, D.H., and Tanaka, K.L., 1986, Geologic map of the western equatorial region of Mars: U.S. Geological Survey Miscellaneous Investigations Series Map I–1802–A, scale 1:15,000,000.

Smith, D.E., Zuber, M.T., Frey, H.V., and 21 others, 2001, Mars Orbiter Laser Altimeter—Experiment summary after the first year of global mapping of Mars: Journal of Geophysical Research, Planets, v. 106, no. E10, p. 23689–23722.

Smith, D., Neumann, B., Arvidson, R.E., Guinness, E.A., Slavney, S., 2003, Mars global surveyor laser altimeter mission experiment gridded data record: NASA Planetary Data System, MGS-M-MOLA-5-MEGDR-L3-V1.0.

Tanaka, K.L., Skinner, J.A., Jr., Dohm, J.M., Irwin, R.P., III, Kolb, E.J., Fortezzo, C.M., Platz, T., Michael, G.G., and Hare, T.M., 2014, Geologic map of Mars: U.S. Geological Survey Scientific Investigations Map 3292, scale 1:20,000,000, pamphlet 43 p., *http://dx.doi.org/10.3133/sim3292*.

Varnes, D.J., 1978, Slope movement types and processes, *in* Schuster, R.L., and Krizek, R.J., eds., Landslides—Analysis and control: Washington, D.C., National Research Council, Transportation Research Board, Special Report 176, p. 11–33.

Witbeck, N.E., Tanaka, K.L., and Scott, D.H., 1991, Geologic map of the Valles Marineris region, Mars: U.S. Geological Survey Miscellaneous Investigations Series Map I–2010, scale 1:2,000,000.

Zurek, R.W., and Smrekar, S.E., 2007, An overview of the Mars Reconnaissance Orbiter (MRO) science mission: Journal of Geophysical Research, v. 112, no. E5, p. 1–22.